RSC Advances

PAPER

View Article Online
View Journal | View Issue

Cite this: *RSC Adv.*, 2026, **16**, 11838

Interfacial defect modulation in hydrothermal CeO_2/graphene nanocomposites for next-generation supercapacitors

Saira,†[a] Hassan Akbar,†[b] Ayesha Bibi,[a] Zeynep Ciğeroğlu,[c] Attaur Rahman,[d] Ali Asghar *[a] and Essam A. Al-Ammar[e]

This study aims to examine the supercapacitor performance of CeO_2/graphene nanocomposites synthesized *via* hydrothermal techniques. X-Ray Diffraction (XRD) results confirmed the successful synthesis of the nanocomposite, with distinct peaks corresponding to the crystalline structure of CeO_2. Transmission Electron Microscopy (TEM) analysis confirmed the uniform distribution of graphene sheets within the CeO_2 matrix, indicating efficient integration of the materials at the nanoscale. The existence of distinctive D (~1350 cm^{-1}) and G (~1585 cm^{-1}) bands, as well as the F_{2g} mode of cubic CeO_2 (~450 cm^{-1}), further validated the successful production of defect-rich graphene using Raman spectroscopy, giving direct spectroscopic validation beyond PXRD analysis. UV-visible spectroscopy revealed characteristic absorption peaks at 323 and 385 nm for pure CeO_2, which shifted to 329 and 375 nm in the composite, indicating modification of defect states at the CeO_2-graphene interface. A significant reduction in optical band gap from 3.21 eV (CeO_2) to 2.75 eV (CeO_2/Graphene) was observed, indicating a modified electrical structure at the interface between graphene and CeO_2. The electrochemical performance of CeO_2 and CeO_2/Graphene was evaluated using CV, GCD, and EIS. CeO_2/Graphene exhibited higher specific capacitance (231 F g^{-1}) than CeO_2 (142 F g^{-1}) in CV, and showed improved cycling stability with a peak capacitance of 285 F g^{-1} in GCD. EIS revealed reduced charge transfer resistance for CeO_2/Graphene, enhancing electrochemical performance. These findings highlight the superior charge storage, energy density (5.7 Wh kg^{-1}), and power density of CeO_2/Graphene, making it a promising material for supercapacitors and energy storage applications.

Received 16th January 2026
Accepted 23rd February 2026

DOI: 10.1039/d6ra00408c

rsc.li/rsc-advances

1. Introduction

The biggest energy problem of the 21st century is the rapidly running out supplies of fossil fuels such as coal, petroleum, and natural gas. Rising global temperatures and growing levels of greenhouse gases in the atmosphere have intensified the energy crisis. This situation demands the development of sustainable energy solutions.[1–4] Electrochemical energy storage devices (EESDs) are highly appealing when it comes to increasing energy sustainability.[4,5] Of these EESDs, supercapacitors (SCs) and second-generation batteries are believed to have made the biggest contributions.[6] Owing to the advanced formulations and high sophistication, rechargeable batteries are incorporated in numerous fields, *i.e.*, portable computers, cell phones, medical equipment and battery-powered cars. However, the commercial adoption of batteries has some disadvantages such as limited life cycles and low power densities. To overcome these constraints, SCs have received considerable attention because of their high power density, minimal maintenance, reasonable price, good safety features, long lifetime, and ability to charge very fast.[7–13] There are two main categories of SCs: electric double layer capacitors (EDLCs) and pseudocapacitors (PCs). Working on non-faradaic processes, EDLCs use carbon-based materials, like activated carbon, reduced graphene oxide, carbon nanotubes, and carbon aerogels as electrodes.[14–17] Conversely, conducting polymers, metallic oxides *i.e.*, NiO, Fe_2O_3, MnO_2, ZnO, Sm_2O_3, CeO_2, and Co_3O_4, as well as acidic oxides, contribute to PCs.[14,15,18,19] A third class is composed of hybrid supercapacitors (HSCs), which combine both operating mechanisms of EDLCs and PCs.[14,20] Of all possible electrode materials, CeO_2 is a good choice because it is inexpensive, environmentally compliant, and has good electrochemical redox properties. Ceria's oxidation state between Ce(III) and

[a]*Department of Physics, The University of Lahore, 1-km, Defense Road, Lahore 54000, Pakistan. E-mail: asghar246@gmail.com*

[b]*Department of Physics, Abbottabad University of Science and Technology (AUST), Abbottabad 22502, Pakistan*

[c]*Department of Chemical Engineering, Faculty of Engineering and Natural Sciences, Uşak University, Uşak 64200, Turkey*

[d]*School of Materials Science and Engineering, Anhui Polytechnic University, Wuhu 241000, China*

[e]*Department of Electrical Engineering, College of Engineering, King Saud University, P.O. Box 800, Riyadh 12372, Saudi Arabia*

† These authors contributed equally to this work.

Ce(IV) encourages electron mobility and the diffusion of cerium ions. Yet, the tendency to agglomerate and inadequate conductive properties provide some obstacles to the ceria's practical use.[17] The integration of graphene seems to provide a promising solution to these limitations. Graphene has an ideal two-dimensional structure for the dispersion of ceria particles and inhibiting their aggregation.[21,22] M. Jayashree *et al.* reported a specific capacitance of 782 F g^{-1} at 2 A g^{-1} current density for their CeO_2/graphene composite. The power and energy densities achieved with the asymmetric device were 2180 W kg^{-1} and 43.5 Wh kg^{-1}, respectively.[23] S Britto and coworkers used an innovative hydrothermal approach for creating high-performance cerium dioxide/graphene nanomaterials as SC electrodes.[24] Additionally, using 5% of CeO_2 content, Yousef *et al.* optimized CeO_2 concentration in graphene nanoflakes and achieved 452.26 F g^{-1} specific capacitance at 0.1 A g^{-1} with improved cycle stability.[25] The majority of research focuses on enhancing CeO_2's electrical conductivity and particle dispersion by graphene integration, even though CeO_2/graphene composites have been previously described for supercapacitor applications. On the other hand, the current study focuses on defect-engineered interfacial coupling, showing how reduction in charge-transfer resistance, bandgap narrowing, lattice microstrain, and oxygen-vacancy modification may all improve electrochemical kinetics. Through quantitative electrochemical kinetic analysis (*b*-value and Dunn's method), UV-vis bandgap assessment, XPS defect evaluation, and Williamson–Hall analysis, this study suggests a structure defect performance relationship, offering deeper mechanistic insight beyond traditional composite fabrication. Our results demonstrated superior electrochemical performance in CeO_2/Graphene nanocomposites, with an energy density of 5.7 Wh kg^{-1} and a corrected specific capacitance of 285 F g^{-1}, which were ascribed to improved charge transfer and decreased internal resistance. In this study, CeO_2 was combined with graphene to improve the electrochemical performance of supercapacitors. The redox properties of CeO_2 and the extraordinary conductivity and surface area of graphene are exploited to reach a feasible pathway towards the production of efficient, low-cost energy storage devices.

2. Experimental section

2.1. Preparation of graphene

Graphene was produced with the electrochemical exfoliation technique. Firstly, a simple setup was used consisting of a graphite rod and steel plate electrodes in a 250 ml Pyrex beaker. Graphite rod was used as positive electrode (anode), and steel plate was used as negative electrode (cathode) in the setup. An electrolyte solution was obtained by dissolving 3.3 grams of $(NH_4)_2SO_4$ in 250 milliliters of deionized water. A low-bias DC source of 12 V was applied to the electrode. The white electrolyte solution then turned into a dark black solution as the bias caused the rods to exfoliate. The process lasted up to 6 h, and the electrolyte solution was becoming denser over time. The exfoliated mixture was eventually coming down to the bottom of the beaker. Repeated washings with deionized water cleaned up the mixture, and filtering took out graphite pieces. To access pure solution, the solution was further sonicated at room temperature for one hour and centrifuged at 5000 rpm for 10 minutes. Finally, the graphene powder was produced after the sample was dried overnight in the furnace at 60 degrees Celsius.

2.2. Synthesis of CeO_2/Graphene composite

The nanocomposites CeO_2/G were synthesized using a hydrothermal approach. A graphene concentration of around 6.5 weight percent (graphene : CeO_2 mass ratio = 1 : 14.3) was achieved by preparing the composite with 0.30025 g of graphene and 4.3028 g of CeO_2. The molar ratio of carbon (from graphene) to CeO_2 was around 1 : 1 according to stoichiometric calculations. Firstly, 0.30025 g of graphene (G) was taken in 25 ml of deionized (DI) water and ultra-sonicated for 30 minutes to ensure the complete dispersion of graphene in the mixture. Secondly, 4.3028 g CeO_2 at 1 M concentration was stirred into another beaker of 25 ml DI water for 30 minutes. Then, the solutions of both beakers were shifted into a single beaker to be stirred magnetically for one hour at 80 °C. After that, the solution was converted into a Teflon-lined autoclave and heated at 180 °C for six hours. After cooling at room temperature, the nanocomposite was gathered, centrifuged and cleaned with DI water numerous times to remove impurities. The dried sample of CeO_2/G composite was obtained by placing the washed material in a drying furnace set at 60 °C for twenty-four hours. Ultimately, grinding was done to turn the dried specimen into a final powdered-form product. This work investigated a single graphene loading (~6.5 weight percent relative to CeO_2; graphene: CeO_2 = 1 : 14.3 by mass) to show how graphene improved defect-mediated electrochemical activity and interfacial charge transfer. Future research will determine quantifiable composition–structure–performance connections and maximize conductive-network creation compared to active CeO_2 consumption by systematically varying graphene concentration under the same synthesis circumstances (Fig. 1).

2.3. Characterization techniques

The prepared graphene, CeO_2, and CeO_2/graphene nanomaterials were analyzed by X-ray diffraction (XRD; PANalytical) using Cu-Kα radiation (λ = 1.5418 Å) over 2θ angle of 10° to 90° to understand crystal structure and phase composition. Transmission electron microscopy (TEM; JEOL JEM-2100) was used to characterize morphological features and the spatial distribution of the materials. Fourier transform infrared spectroscopy (FTIR; Bruker Vertex 70) in the range of 4000–500 cm^{-1} was used to investigate the molecular structure and chemical bonding. Raman spectroscopy (λ = 532 nm) was used to validate graphene production and study oxygen-vacancy-related vibrations in the CeO_2/Graphene composite. UV visible spectroscopy (UV-vis; Shimadzu UV2600) was used to analyze optical and electronic transitions over wavelength range from 200 to 800 nm.

2.4. Electrochemical super-capacitor electrode preparation

The working electrode is made-up as follows, firstly as synthesized electroactive material (wt. = 80%), porous activated

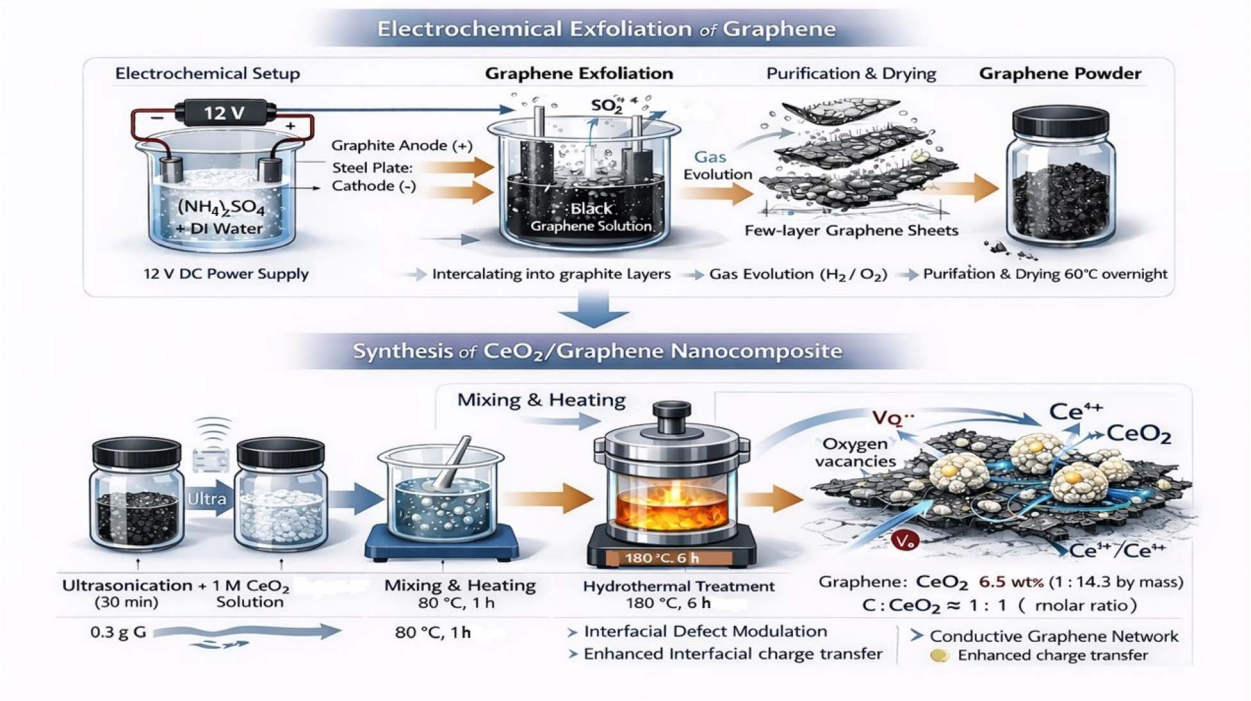

Fig. 1 Schematic illustration of electrochemical exfoliation of graphene and subsequent hydrothermal synthesis of CeO_2/Graphene nanocomposites, exhibiting interfacial defect modification and improved charge-transfer routes.

carbon along with polyvinyldine fluoride (PVDF) is use with the ratio (wt. = 10%) each and dissipating these in NMP for making the continuous homogenous mixture. Analytical balancing was used to accurately quantify the quantity of active material deposited on each nickel foil electrode. The average active mass loading was around 3 mg per electrode, or 1.5 mg cm^{-2},and the same loading was used for all mass-normalized electrochemical calculations. Secondly the nickel foil is to be cut into the area of (1 × 2 cm^2) before depositing the slurry, the nickel foil is washed with ethanol in ultrasonicated machine for 1 h to purify it from the external impurities and let them dry for 24 h at 60 °C in dry oven. Lastly, making the electrode for supercapacitor application, the prepared slurry of electroactive material is to be deposited on the nickel foil with the micropipette (10–100 μl) with very carefully and precisely by coating method. After deposition the electrode was kept at 60 °C in oven for overnight. The electrochemical analysis to be performed by electrochemical analyzer (CORRTEST instrument Model CS350M) with 3 different electrodes setup in which Ag/AgCl is a reference electrode, platinum wire as a counter electrode and electroactive material as a working electrode in 1 M KOH aqueous electrolyte solution. The electrochemical characterization was performed by means of cyclic voltammetry (CV) with potential range of 0–0.8 V at different scan rate (mV s^{-1}) from 5–80 respectively, and Galvanic charging–discharging (GCD) with applied potential of 0.8 V at different current densities (0.8–1.4 A g^{-1}) to investigate electrochemical properties. Electrochemical impedance spectroscopy (EIS) was performed in 100 kHz to 0.01 Hz range of frequency at alternative current voltage of 5 mV.

3. Results and discussion

3.1 XRD characterization

The XRD technique was conducted to analyze the crystal structure of CeO_2/Graphene composites. Its diffraction behaviour is illustrated in Fig. 2(a). The graph shows eight characteristic peaks of cerium oxide, located at $2\theta = 28.3°$, 34.3°, 47.5°, 55.6°, 60.0°, 69.0°, 75.2° and 79.0°. These peaks were labelled as (111), (200), (220), (311), (222), (400), (331), and (420) respectively, by following their correspondence to JCPDS card # 34-0394. These indices ensured the presence of crystalline cubic fluorite-structured ceria in the composite. The phase purity of the synthesized CeO_2 was confirmed by the presence of all of these characteristic peaks with no impurity reflections.[26] The most intense peak at 28.3° related to the (111) plane demonstrated the preferential orientation for CeO_2. It verified the creation of short grains with small-size attributes of cerium oxide. However, when we compare graphene's (006) peak from JCPDS no. 26-1076 to the composite peaks, it can be seen that this peak is shifted to the lower angle. The reason behind this shifting might be the thermal stress or the difference in thermal expansion coefficients of graphene and CeO_2 during the composite's synthesis mechanism.[27,28] The reduced grain growth improving the overall performance of super-capacitors.[29,30] Furthermore, overlapping low-intensity reflections and/or a modest desired orientation may result in weak features in the composite pattern. Crucially, rather than being measured by the existence of extra peaks, the reduction in crystallite size is demonstrated by peak widening and is measured using the Scherrer and Williamson Hall analyses. This interpretation is in

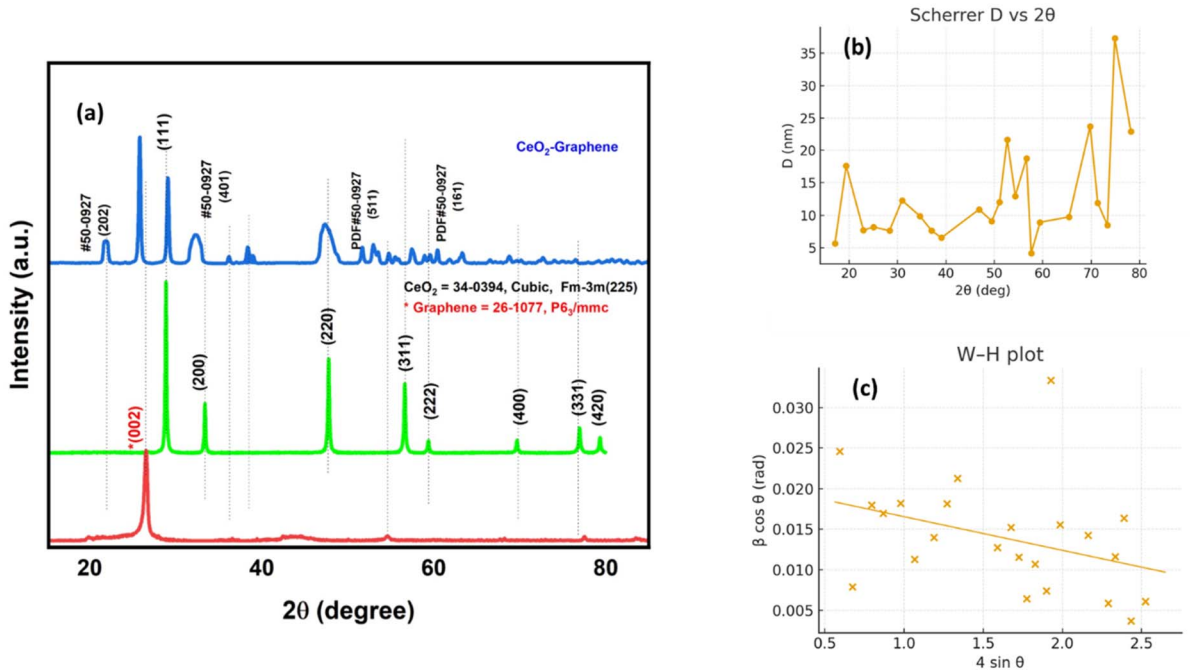

Fig. 2 (a) X-ray diffraction pattern, (b) crystallite size and (c) Williamson–Hall (W–H) plot of graphene and CeO_2/Graphene.

accordance with the Scherrer and Williamson–Hall studies' measurements of the CeO_2/Graphene composite's increased full width at half maximum (FWHM) of the dominant (111) reflection while compared to pure CeO_2.The Scherrer equation was used to determine the samples' crystallite size (Fig. 2(b)). While compared to pure CeO_2, the CeO_2/Graphene composite exhibits larger diffraction peaks and a lower crystallite size, indicating reduced grain development caused by graphene sheets. The electroactive surface area is increased and quicker redox reactions are supported by this nanoscale size improvement. The peak broadening is further divided into size and strain contributions using the Williamson–Hall (W–H) plot (Fig. 2(c)). The existence of extra lattice microstrain caused by the CeO_2–graphene interface and defect development (oxygen vacancies) is confirmed by the CeO_2/Graphene sample's larger positive slope. Together, the decreased crystallite size (intercept) and increased microstrain (slope) show that the addition of graphene creates advantageous structural distortions that complement the composite's enhanced electrochemical performance.

3.2. SEM analysis

Scanning electron microscopy (SEM) was used to analyze the surface morphology of the prepared CeO_2 and CeO_2/Graphene samples, as shown in the Fig. 3(a–c). CeO_2 has an agglomerated morphology, indicating that dense secondary particles form when short grain clusters come together. The XRD data, which verified the cubic fluorite phase with comparatively tiny crystallite sizes, are consistent with this observation. While CeO_2 nanoparticles have a high surface energy, the aggregation propensity is predicted. A distinct change in morphology is seen with the addition of graphene. When graphene is added, CeO_2 nanoparticles show better dispersion and less aggregation than pure CeO_2, suggesting a modification of the surface morphology shown in Fig. 3(b and c). The presence of graphene likely influences the dispersion and spatial distribution of CeO_2 nanoparticles, leading to reduced aggregation, as shown by the changed surface texture. A more evenly dispersed nanostructure is probably the result of severe aggregation being suppressed and excessive particle development being limited by the existence of a supporting framework. The altered surface morphology and decreased particle crowding suggest graphene's structural effect inside the composite, despite the fact that its ultrathin and electron-transparent nature makes it difficult to see clearly in SEM images. As covered in the next section, HRTEM investigation further validates the nanoparticle anchoring and detailed interfacial characteristics.

3.3. HRTEM analysis

TEM images of the CeO_2/G nanocomposite in Fig. 4(a and b) illustrate that the CeO_2 nanoparticles are well distributed over the graphene sheets and nearly spherical, forming a well-distributed nanostructured composite. CeO_2 particles range in size from approximately 10 and 30 nm, with an average size of around 20.4 $\pm$ 4.0 nm, as determined by the particle size distribution histogram from HRTEM (Fig. 4(d)), indicating a nanoscale shape that is compatible with effective interfacial contact between CeO_2 and the graphene substrate. Distinct lattice fringes with interplanar spacing of 0.28 nm and 0.19 nm, which correspond to the (200) and (220) planes of cubic CeO_2, respectively, are observed in high-resolution HRTEM (Fig. 4(c and d)) demonstrating the significant crystalline structure of

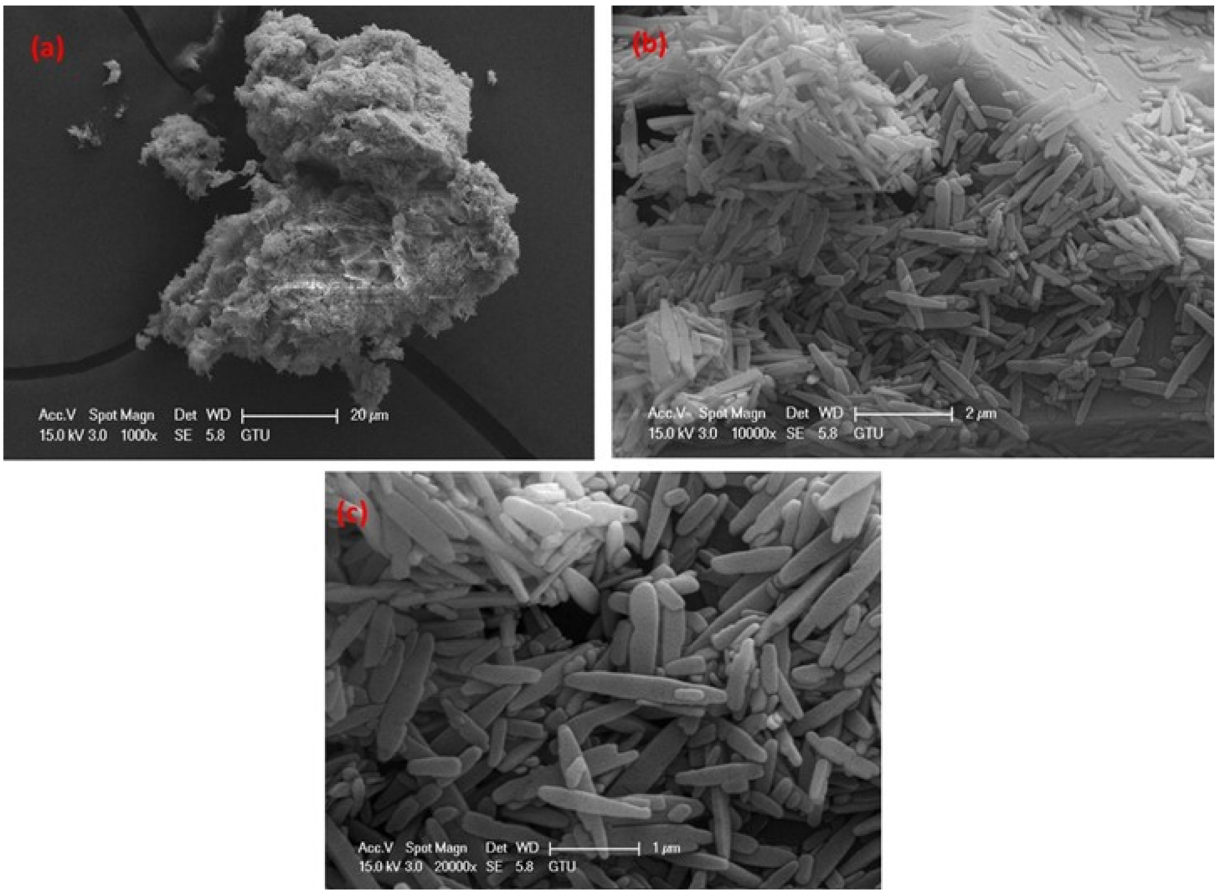

Fig. 3 SEM images showing the morphological characteristics of (a) pure CeO_2 displaying porous, agglomerated clusters, (b) CeO_2/Graphene nanocomposite exhibiting CeO_2 grains dispersed across a rough, textured background, and (c) high-magnification SEM image of the CeO_2/Graphene nanocomposite.

the nanoparticles.[31] The crystalline fluorite structure is further supported by the well-defined diffraction rings indexed to the (111), (200), (220), (311), and (331) planes of CeO_2 in the selected-area electron diffraction (SAED) pattern Fig. 4(c). The X-ray diffraction (XRD) Fig. 1 results, which show precise reflections corresponding to the (111), (200), (220), (311), (222), (400), (331), and (420) planes of cubic CeO_2 (JCPDS No. 34–0394), support the *Fm*-3*m* space group and are in perfect alignment with these microscopic observations.[30,32] Also the graphitic phase of graphene (JCPDS no. 26-1077) is accountable for a weak and broad diffraction feature in the XRD pattern that is centred at about 26° (002), indicating the presence of few-layer or weakly crystalline graphene. A strong interfacial contact between CeO_2 nanoparticles and the underlying graphene sheets has been demonstrated in the TEM and HRTEM images, suggesting efficient dispersion within the composite structure.[33]

3.4. FTIR spectroscopic analysis

Fig. 5(a) shows unique vibrational patterns for pristine CeO_2 nanoparticles and CeO_2/Graphene nanocomposite. The pure CeO_2 FTIR exhibits several characteristic peaks. The peak at 1634 cm^{-1} can be attributed to the effect of surface carbonyl groups or adsorbed species, whereas the wide band at 3435 cm^{-1} is ascribed to O–H stretching vibrations connected to surface hydroxyl groups or adsorbed moisture. The successful formation of the metal oxide structure was evidenced by the vibrational modes of Ce–O bond stretching at 659 cm^{-1} and 722 cm^{-1}. The FTIR spectrum of the CeO_2/Graphene nanocomposite was found to be more complex, verifying interaction between the components. The CeO_2/Graphene composite's FTIR spectrum shows additional bands in the 1500–1400 cm^{-1} region (1511 and 1437 cm^{-1}). These bands can be attributed to surface-adsorbed species introduced during processing or vibrations of oxygen-containing carbon functionalities (such as carboxylate/carbonate-related modes) on the graphene surface. However, FTIR by itself is unable to definitively validate particular coordination geometry or the production of Ce–O–C bonds, despite these characteristics suggesting an interfacial contact between CeO_2 nanoparticles and oxygen-functional groups on graphene. Consequently, we do not consider these bands to be definitive confirmation of a specific bidentate coordination structure, but rather suggest surface functional-group interaction. This interpretation is consistent with the oxygen-functionalized carbon species identified in the XPS C 1s and O 1s spectra. In addition, the spectrum gave graphene

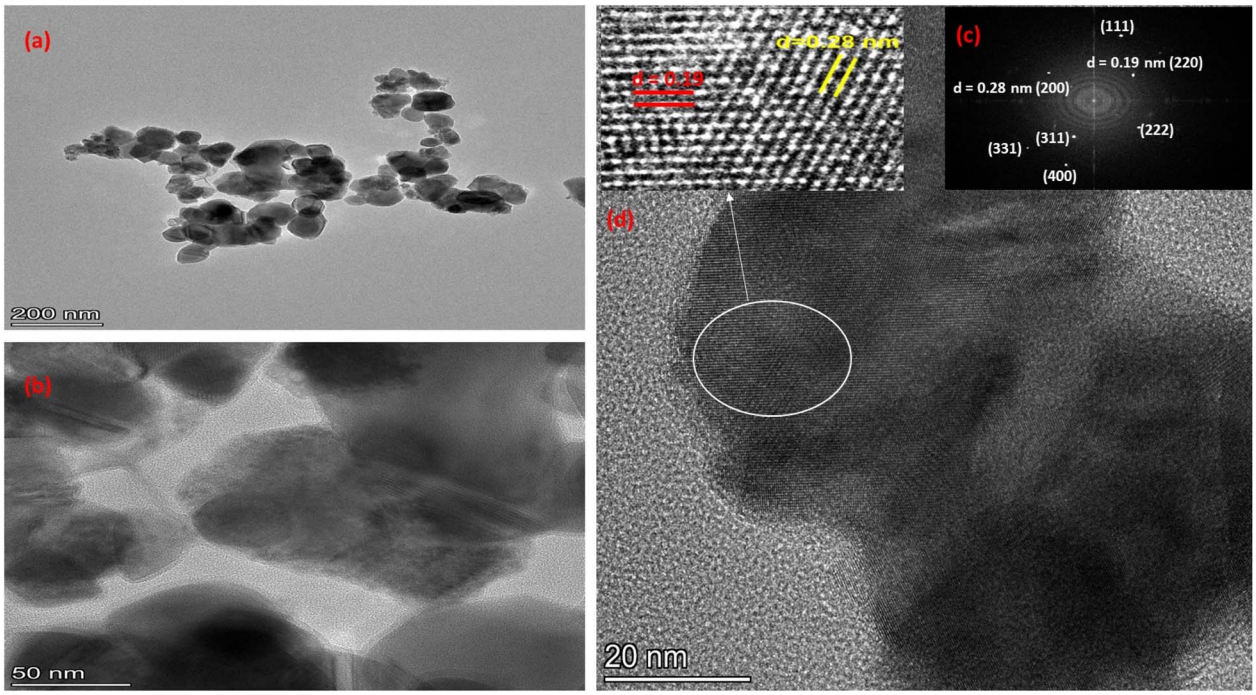

Fig. 4 TEM, HRTEM, and SAED analysis of the CeO_2/Graphene nanocomposite (a and b) low and high-magnification TEM images, (c) SAED pattern indexed to cubic CeO_2, and (d) HRTEM image showing lattice fringes of 0.28 nm (200) and 0.19 nm (220), with the circled region indicating the graphene sheet.

related peaks at 1386 cm^{-1} (O–H deformation), 1219 cm^{-1} and 1112 cm^{-1} (C–O stretching), indicating the presence of several oxygen functional groups. The retention of the 659 cm^{-1} peak indicates that the Ce–O framework was retained in the composite structure. Additional weak bands at 1993 cm^{-1} and 804 cm^{-1} might be the result of surface-associated species or minor structural changes made during the creation of the composite. Although these characteristics raise the possibility of interfacial contact, they do not prove a strong chemical binding on their own.[34–36] To verify that graphene produced by electrochemical exfoliation had been successfully produced, Raman spectroscopy was employed. The CeO_2/graphene composite's Raman spectra (Fig. 5(b)) shows two strong peaks that are located at around ~1350 cm^{-1} (D band) and ~1585 cm^{-1} (G band). The disorder-induced breathing mode of sp^2 carbon rings gives birth to the D band, whereas the in-plane E_{2g} vibrational mode of sp^2-hybridized carbon atoms is represented by the G band. The formation of graphitic carbon is fully confirmed by the existence of these well-resolved D and G bands.[37] As is typical of graphene produced by electrochemical exfoliation, the computed intensity ratio ($I_D/I_G \approx 1.0$) shows the existence of edge sites and structural defects. Ion intercalation

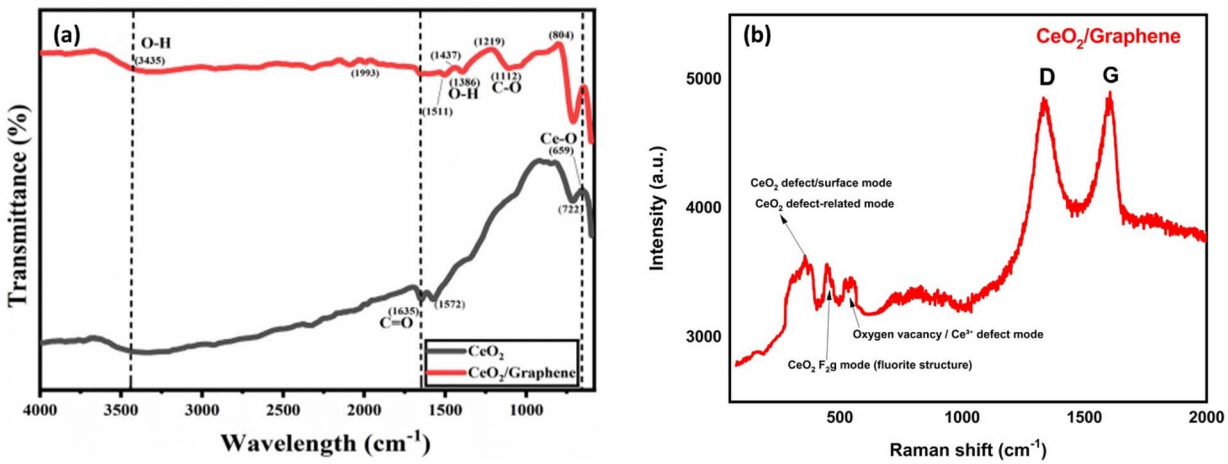

Fig. 5 (a) FTIR spectrum of CeO_2 and CeO_2/Graphene nanocomposite, (b) Raman spectra of CeO_2/Graphene nanocomposite.

and oxidation activities that take place during exfoliation are predicted to produce few-layer, edge-dominated graphene sheets with such defect-rich characteristics. The F_{2g} symmetric stretching mode of cubic fluorite CeO_2 is identified by a prominent band at around 450 cm^{-1} in the low-wavenumber region, indicating that the crystalline structure of the material has been preserved inside the composite. Lattice deformation and defect formation are indicated by additional characteristics in the 520–560 cm^{-1} range that are ascribed to oxygen-vacancy-related and Ce^{3+}-associated defect modes. The surface and symmetry-breaking effects characteristic of nanocrystalline CeO_2 are further supported by weak bands at between 357 and 380 cm^{-1}.[38] The results overcome the limitations of PXRD alone and confirm the effective synthesis of the CeO_2/graphene composite by offering direct spectroscopic evidence for both defect-rich graphene production and oxygen-vacancy-containing CeO_2.

3.5. XPS analysis

The CeO_2/G sample's X-ray photoelectron spectroscopy (XPS) survey spectrum (Fig. 6(a)), which has peaks attributed to Ce 3d, O 1s, and C 1s, indicates the presence of Ce, O, and C as the primary elements. Gaussian–Lorentzian peak fitting with Shirley background correction was used to deconvolute high-resolution spectra in order to determine which chemical states were present in the composite. Table 1 provides the fitting parameters, which include the deconvoluted components' relative peak areas, FWHM values, and binding energies. The XPS survey spectrum was used to quantify the elemental composition on the surface. Significant ceria loading on the graphene support was confirmed by the atomic concentrations of around Ce ≈ 33 at%, O = 34 at%, and C ≈ 36 at%. As further confirmed by the Ce 3d fitting, the resultant Ce/O atomic ratio is close to unity (Ce/O = 0.97), which is compatible with the generation of CeO_2 and the presence of oxygen-deficient surface species (Ce^{3+}/oxygen vacancies). The usual multiples structure of Ce^+ is shown by high-resolution investigation of the Ce 3d region (Fig. 6(b)). This structure is composed of the through the different v and u spin–orbit components, which are observed in the 882–917 eV range. The deconvoluted Ce 3d spectrum indicates six major peaks (v_0, v, v'', u_0, u, and u''), which are characteristic of Ce^{4+} in CeO_2, showing that cerium usually exists in the +4 oxidation state.[39] A slight contribution from Ce^{3+} may be present, as evidenced by minor low-intensity patterns, suggesting a small number of oxygen vacancies, which is frequent in CeO_2/graphene composites. The O 1s spectrum (Fig. 6(c)) displays a prominent peak near ~530.0 eV due to lattice oxygen (O^{2-}) in CeO_2, combined with a higher binding-energy shoulder that can be attributed to surface hydroxyl or adsorbed oxygen species, the O 1s spectrum was resolved into two main

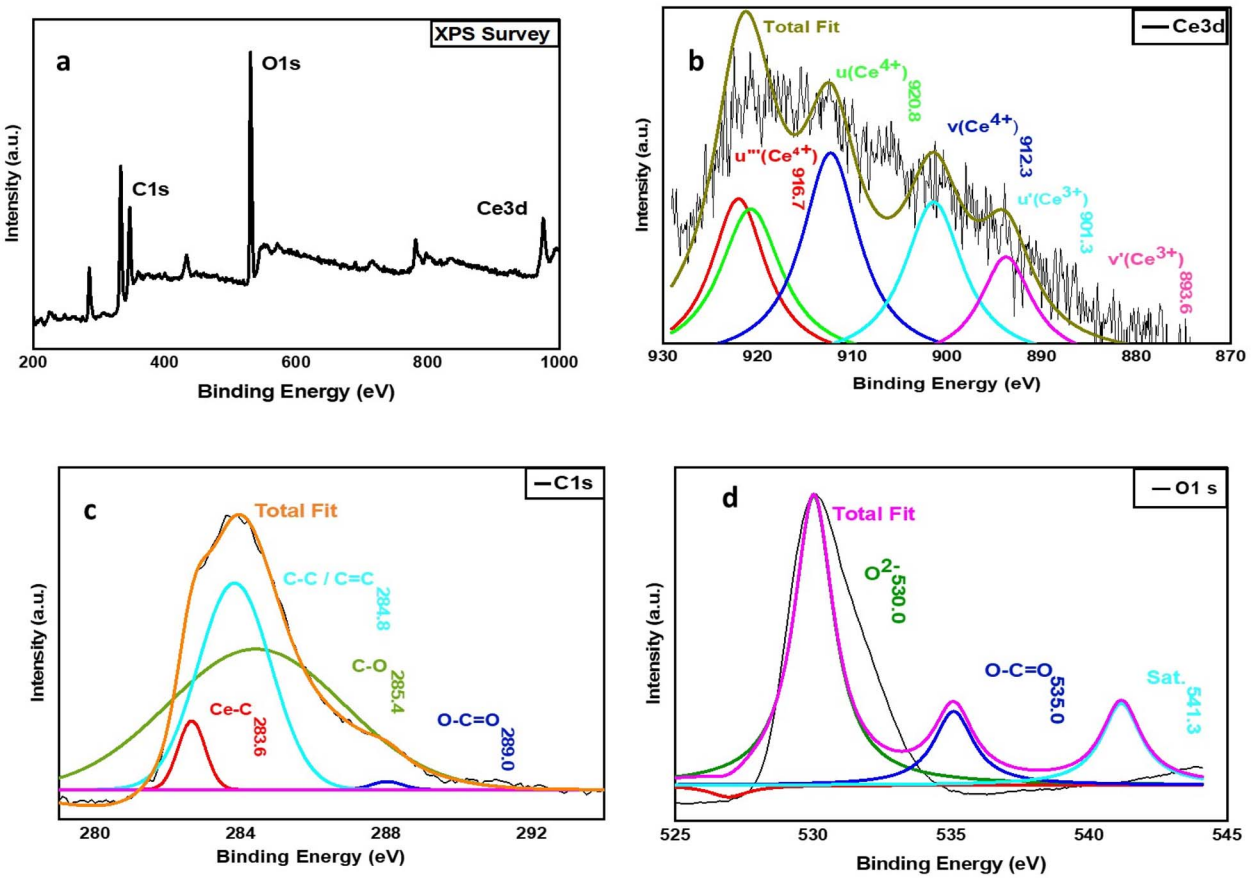

Fig. 6 XPS analysis of the CeO_2/graphene nanocomposite: (a) survey spectrum, (b) high-resolution Ce 3d spectrum, (c) high-resolution C 1s spectrum, and (d) high-resolution O 1s spectrum.

Table 1 Fitting parameters for high-resolution XPS spectra (Ce 3d, O 1s, and C 1s) of CeO_2/Graphene nanocomposite

S.no	Name	Start BE	Peak BE	End BE	Height CPS	FWHM eV	Area (*P*) CPS.eV	Area (*N*) TPP-2M	Atomic%
1	C1s	296.98	284.8	278.18	51 451.1	3.258	202 005.06	2832.59	36.01
2	O1s	543.98	530.14	524.18	267 528.9	3.016	869 039.89	5034.49	33.99
3	Ce	918.23	876.98	880	567 328.2	3.104	826 003.91	6533.68	32.99

components centered at ~529.5 eV (lattice oxygen, Ce–O) and ~531.5–532.0 eV (surface hydroxyl or defect-related oxygen species). The C 1s spectrum reveals peaks that indicate graphitic carbon (~284.8 eV) and oxygen-functionalized carbon species at higher binding energies, confirming the presence of graphene and surface oxygen groups, the C 1s spectrum (Fig. 6(d)) was deconvoluted into distinct components at ~284.8 eV (C–C/C=C), ~285.6 eV (C–O), and ~288.5 eV (O–C=O), confirming the presence of graphitic carbon and oxygen-containing functional groups. The present data verify the effective production of CeO_2 on the graphene support and the majority of Ce^{4+} species with small oxygen-deficient Ce^{3+} locations.[40]

3.6. UV analysis

The optical distinctive behaviour of both CeO_2 and CeO_2/Graphene composite was observed using UV visible spectroscopic analysis represented in Fig. 7(a and b). Two characteristic absorption peaks at 323 and 385 nm were exhibited by pure CeO_2. The peak at 323 nm was attributable to charge transfer transitions from O2p to Ce4f states. While the 385 nm peak was associated with transitions modified by oxygen vacancies and Ce^{3+} states. The nanocomposite formation of CeO_2/Graphene showed a significant peak shift to 329 and 375 nm respectively. An enhanced electronic coupling between CeO_2 and graphene components to yield optimized charge transfer pathways was evidenced by the red shift of the 323 nm peak to 329 nm. Simultaneously, the blue shift of the 385 nm peak to 375 nm indicated increased oxygen vacancy concentration at the interface that provided additional redox active sites for charge storage to boost specific capacitance.[41–43] By use of Tauc plots, the optical band gap energies were calculated and found to decrease significantly from 3.21 eV for pure CeO_2, to 2.75 eV for CeO_2/graphene composite. The reduction in band gap energy can be explained as a result of introducing new electronic states at CeO_2-graphene interface along with the improved charge transfer channels associated with the graphene's high electrical conductivity. The electronic structure modifications imply improved charge transfer capabilities, as desired to enhance supercapacitor performance.[44]

4. Electrochemistry performance

4.1. CV of CeO_2 and CeO_2/Graphene

Cyclic voltammetry (CV) test is performed, by applied potential window between 0–0.38 V at a different scan rate from 5 mV s^{-1} to 80 mV s^{-1} at room temperature. Fig. 8 (a) CeO_2, (b) CeO_2/Graphene, both CV profile shows the quasi-rectangular redox peaks which indicating the well suited pseudocapacitive

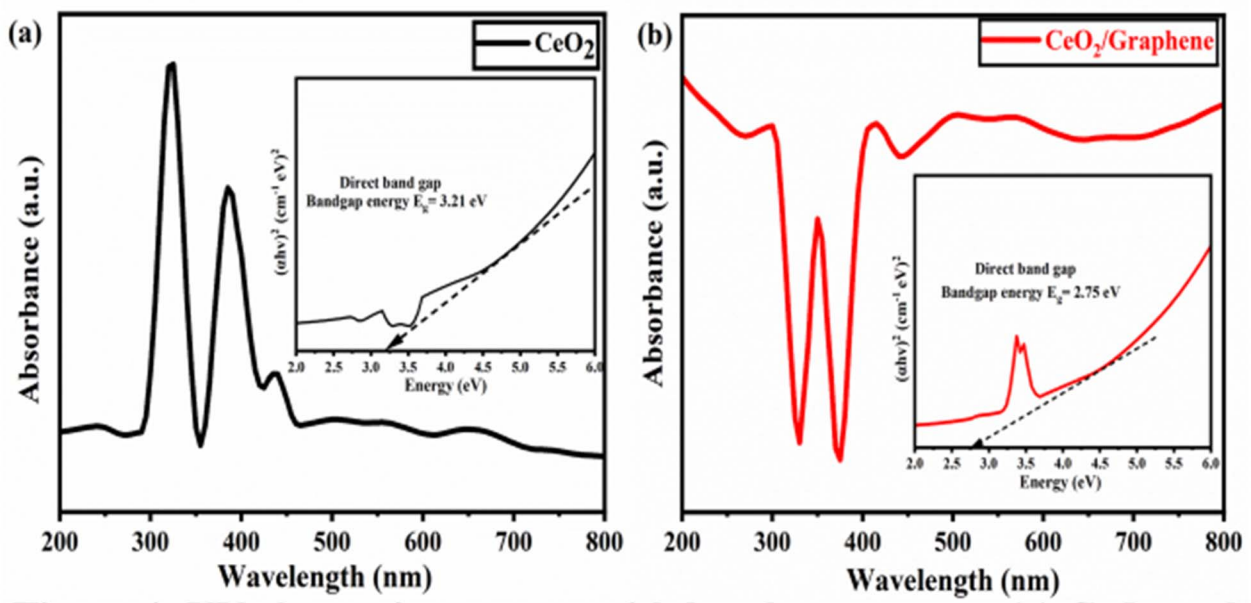

Fig. 7 UV absorption spectra with band gap energies; (a) CeO_2 and (b) CeO_2/Graphene nanocomposite.

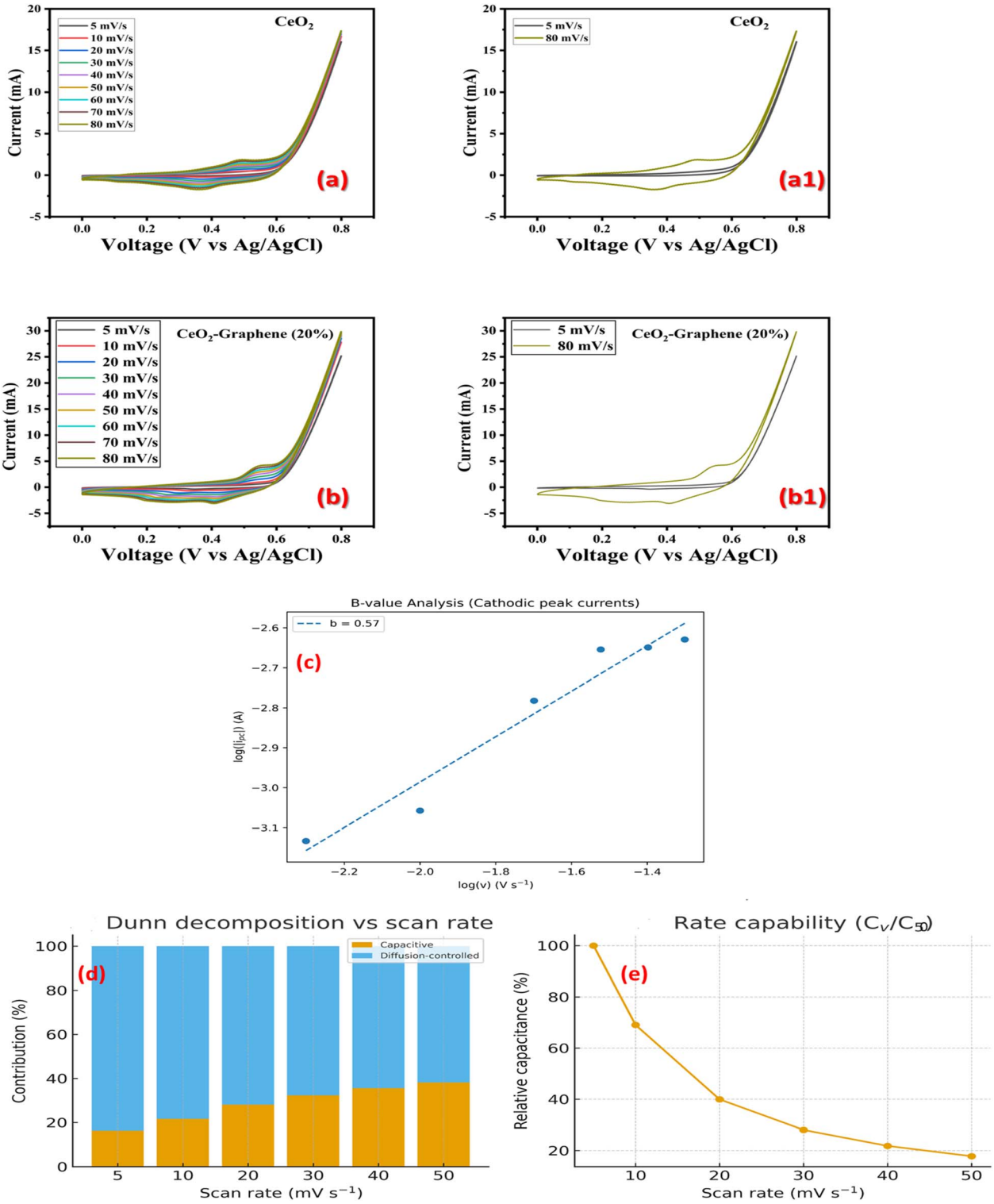

Fig. 8 Cyclic voltammetry curve of (a and a1) CeO_2, (b and b1), (c) *b*-value analysis, (d) Dunn's method decomposition at 40 mV s^{-1}, and (e) capacitive contribution *vs.* scan rate for CeO_2/Graphene.

behaviour showing better reversibility and excellent faradaic redox reaction response with respects to different scan rates range between the 0–0.8 V potential window. Positively shifted peak potential in range of 0.4–0.6 V is for the anodic and between 0.2–0.4 V negatively shifted potential peaks indicate the cathodic corresponding to the reversibility of $Ce^{4+} \leftrightarrow Ce^{3+}$ redox transitions.[23,45] The CeO_2/Graphene electrode shows increased redox peak currents and an insignificant extra feature at ~0.4 V when compared to pure CeO_2. This can be attributed to defect-related oxygen functions at the CeO_2–graphene

interface and better electronic conductivity. The related log (i)–log (v) graphs (Fig. 8(c)) The pure CeO_2 electrode's b-value of 0.54 and 0.53 for CeO_2/Graphene suggests that diffusion-controlled faradaic redox processes corresponding to reversible $Ce^{4+} \leftrightarrow Ce^{3+}$ transitions are primarily responsible for charge storage. CV curves obtained at various scan rates were used to precisely determine the capacitive and diffusion-controlled contributions to charge storage using Dunn's approach (Fig. 8(d and e)).[46] The capacitive contribution of CeO_2 was approximately 37.5% at a typical scan rate of 40 mV s^{-1}, whereas diffusion-controlled mechanisms accounted for approximately 62.5% of the overall charge storage. The capacitive contribution for the CeO_2/Graphene electrode increased to around 39.1%, demonstrating improved surface-controlled charge storage is attainable by the framework with conductive graphene. The CeO_2/Graphene composite exhibited a similar b-value of 0.53 (R^2 = 0.997) following graphene integration. Nonetheless, the conductive graphene framework greatly improves interfacial charge transport and electrochemical usage of active sites, evidenced by the greater current response, decreased charge-transfer resistance shown in EIS, and improved capacitive contribution from Dunn's study. In keeping with kinetically restricted ion diffusion at higher sweep rates, the rate-capability investigation (Fig. 8(e)) demonstrates a gradual decrease in relative capacitance with scan rate. Enhanced interfacial charge transport in the CeO_2/Graphene electrode is confirmed by these kinetic results, which are in agreement with the decreased charge-transfer resistance shown in EIS.

The specific capacitance of electrode was formulated by the following equation:

$$C_{sp} = \frac{1}{m \cdot v \cdot \Delta V} \int_{v_i}^{v_f} I \times V \mathrm{d}V \quad (1)$$

Here, specifics capacitance is denoted by (C_{sp}), active mass in mg of electrode material is denoted by (m), v is scan rate, ΔV is potential window and $\int I(v)$ give the cyclic voltammetry current curves. In Fig. 9, the highest specific capacitance of pure CeO_2 is 142 F g^{-1} at 5 mV s^{-1}. At the same scan rate the CeO_2/Graphene nanocomposite electrode specific capacitance value were found to be 231 F g^{-1}. Despite having a lower inherent gravimetric capacitance than CeO_2 in pseudocapacitive systems, graphene does not simply dissolve the active material when added at a relatively low proportion (~6.5 wt%). If there were no synergistic effect, such a modest carbon proportion would significantly reduce the mass-normalized capacitance, as expected by a rule-of-mixtures. However, by enhancing charge transfer and decreasing polarization losses, graphene functions as a conductive percolation framework that raises CeO_2's electrochemical utilization factor (η). Redox site accessibility and ion diffusion kinetics are improved by the reported decrease in charge-transfer resistance, reduction in crystallite size, higher microstrain, and enhanced oxygen-vacancy concentration. The minor dilution impact is surpassed by these synergistic interfacial effects, which raises the composite specific capacitance overall. The highest specific capacitance values for nanocomposite is attributed due to the incorporation of graphene which enhanced its conducting surface area property for the ions between the electrode and electrolyte solution respectively. The exact same active mass, voltage window (0–0.8 V), and discharge duration requirements were used in both CV and GCD studies to ensure uniformity. The reference baseline for verifying the GCD-derived C_{sp} was the recalculated CV-derived capacitance values.[33,47]

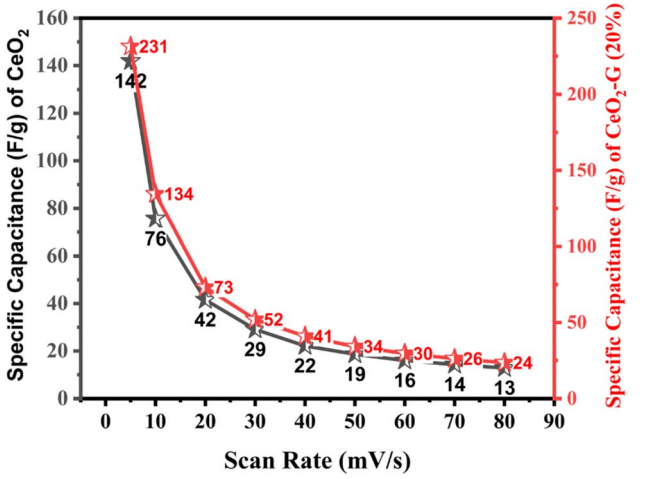

Fig. 9 Specific capacitance (C_{sp}) (F g^{-1}), relationship with different scan rates formulation.

4.2. Galvanic charging–discharging (GCD)

The electrochemical performance of electrode material bare CeO_2 and CeO_2/Graphene nanocomposite is further investigated by Galvanic charging–discharging (GCD) characterization with respect to varying current densities from 0.8 A g^{-1} to 1.4 A g^{-1} with the applied potential of 0.8 V respectively. Fig. 10(a and b) clearly demonstrating the GCD behaviour of both electrodes material with slightly voltage drop as the current density increases from 0.8 A g^{-1} to 1.4 A g^{-1}. From the GCD consistence shape the good symmetric behaviour proposing the good reversibility of redox abilities and pseudocapacitance charge storage nature dominance can be seen which clearly agree well with the CV results.

The specific capacitance (C_{sp}) values can be formulated by the following equation as given below:[30]

$$C_{sp} = \frac{I \times \Delta t}{m \times \Delta V} \quad (2)$$

Here, I/m shows the current density (A g^{-1}), Δt is given as discharging time of electrode and ΔV is the potential applied during GCD test.

The CeO_2 and CeO_2/Graphene electrodes were investigated using galvanostatic charge–discharge (GCD) experiments at different current densities in the potential range of 0–0.8 V *versus* Ag/AgCl. The internal resistance of the electrode–electrolyte interface is responsible for the noticeable voltage drop (IR-drop) that occurs at the beginning of each discharge curve (Fig. 10(c)). Due to increased ohmic losses at increasing charge-transfer rates, the IR-drop's magnitude increases with current

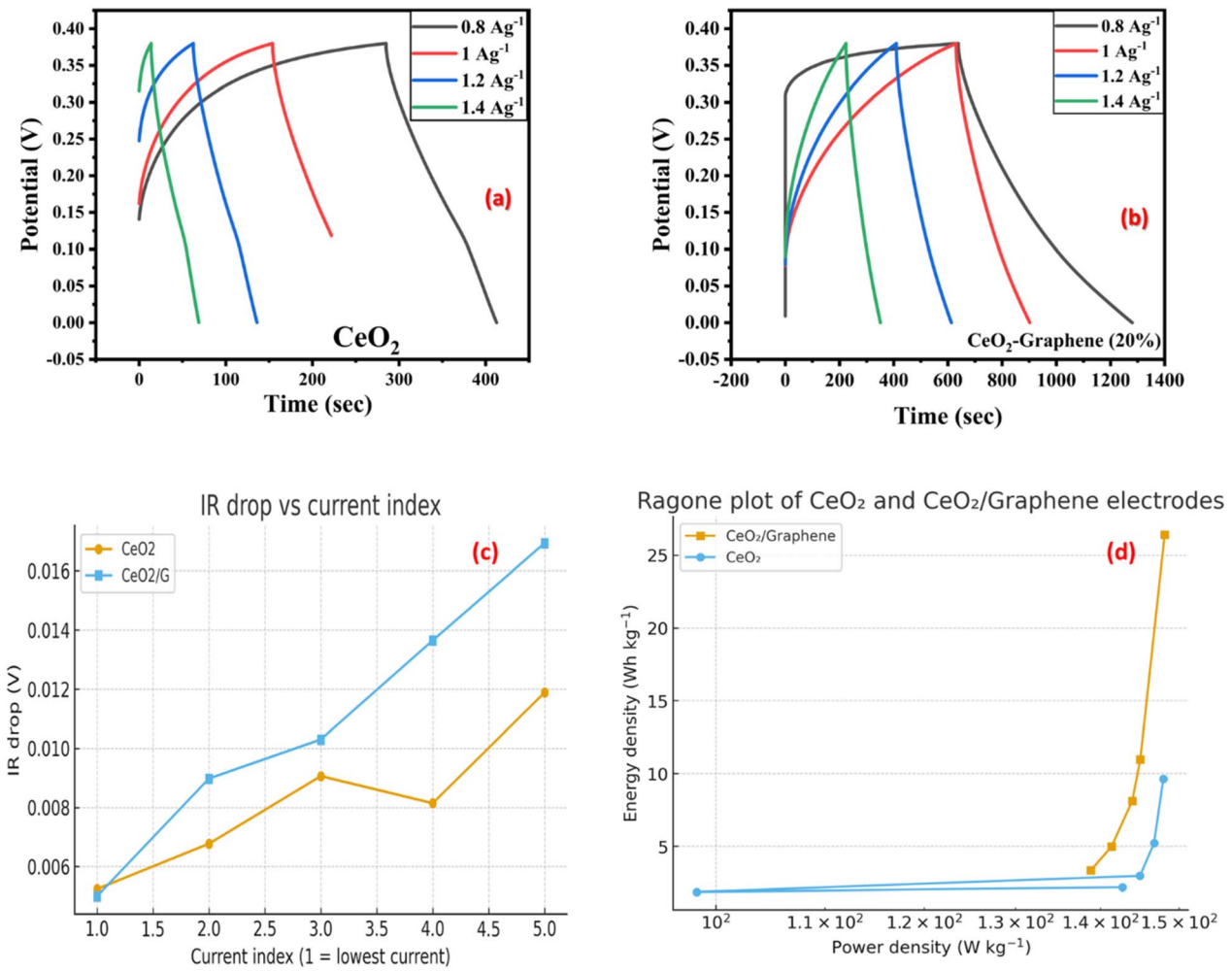

Fig. 10 Galvanic charging–discharging test (GCD) of (a) CeO_2, (b) CeO_2/Graphene, (c) IR drop and (d) Ragone plot of CeO_2 and CeO_2/Graphene nanocomposite.

density as predicted. For the pure CeO_2 electrode, the IR-drop rises from around 0.005 V at the lowest current to about 0.012 V at the highest current density. The CeO_2/Graphene composite shows a similar growing trend with values between ~0.005 V and ~0.017 V. The equivalent series resistance (ESR) of the electrode–electrolyte system is the source of the initial voltage drop (IR-drop) observed at the initial point of each discharge curve, which rises with current density as a result of increased ohmic losses. The generally minimal IR-drop values indicates good electrical connection and moderate series resistance in both systems, however the CeO_2/Graphene electrode exhibits a slightly greater IR-drop at higher current densities, which may be caused by electrode thickness or contact resistance. The energy density (E, Wh kg^{-1}) and power density (P, W kg^{-1}) were calculated using the discharge time (Δt) and effective operating voltage ($V_{eff} = \Delta V - IR$) according to:

$$E = \frac{C_{sp} \times \Delta V^2}{2 \times 3.6} \quad (3)$$

$$P = \frac{E \times 3600}{\Delta t} \quad (4)$$

The GCD-derived specific capacitance values were used to reconstruct the Ragone properties of both electrodes (Fig. 10(d)). At 0.8 A g^{-1}, pure CeO_2 possesses a maximum energy density of 3.3 Wh kg^{-1}, which decreases at higher currents due to a shorter discharge duration. The CeO_2/Graphene composite produces an energy density of 5.7 Wh kg^{-1} at a power density of 190 W kg^{-1}, even though it operates within the same restricted potential window (0–0.8 V). Because the graphene network reduces charge-transfer resistance and speeds up ion transport, the composite exhibits enhanced power-handling capability. The changed discharge time (Δt), accurate mass loading in accordance with CV measurements, and an effective voltage window of $\Delta V = 0.8$ V were used to determine the GCD-derived specific capacitance in Fig. 11. In good agreement with the CV-derived value of 142 F g^{-1}, the CeO_2 electrode produced a specific capacitance of 165 F g^{-1} at 0.8 A g^{-1}, which dropped to 118 F g^{-1} at 1.4 A g^{-1}. The CeO_2/Graphene composite, in comparison, showed higher specific capacitances of 285 F g^{-1} at 0.8 A g^{-1} and 192 F g^{-1} at 1.4 A g^{-1}, which were corresponding with its CV-derived capacitance of 231 F g^{-1}. The conductive graphene structure, which promotes

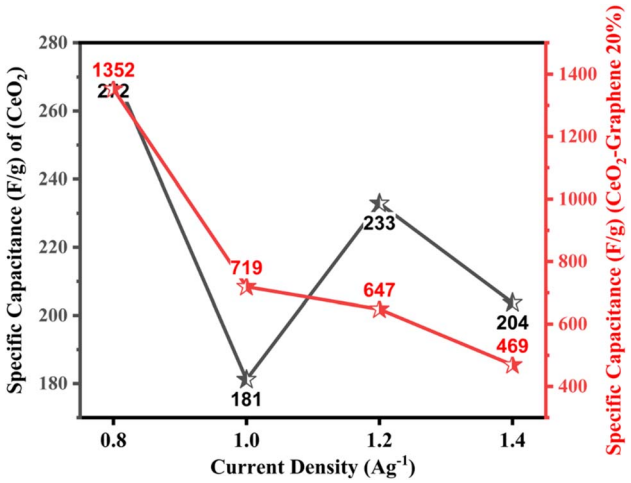

Fig. 11 Specific capacitance C_{sp} (F g^{-1}) at different current densities (0.8–1.4 A g^{-1}).

quick electron transit and improved ion diffusion, is responsible for the increased charge storage capacity.

Along with that the leading analysis of electrochemical characterization two of the more key assessment for their performance are energy density (E_d) and power density (P_d) at the same considerable values at current density range (0.8–1.4 A g^{-1}) for the bare CeO_2 and CeO_2/Graphene.[48] Both the density values are formulated by the eqn (3) and (4). The energy density (E) and power density (P) values for CeO_2 and CeO_2/Graphene are displayed in Fig. 12a and b. At 0.8 A g^{-1}, CeO_2 exhibits a maximum energy density is 3.3 Wh kg^{-1}. Based on the corrected C_{sp} and the effective discharge voltage, the CeO_2/Graphene electrode offers an energy density of 5.7 Wh kg^{-1} at a power density of 190 W kg^{-1}.

4.3. Electrochemical impedance spectroscopy (EIS)

The charge-transfer kinetics and ion transport characteristics at the electrode–electrolyte interface were examined using electrochemical impedance spectroscopy (EIS). A three-electrode setup in a 1 M KOH aqueous solution was used to conduct measurements in the frequency range of 100 kHz to 0.01 Hz. The Nyquist plots of the CeO_2 and CeO_2/Graphene electrodes, along with the fitted curves produced by ZSimDemo 3.20, are shown in Fig. 13(a and b), demonstrating a strong agreement between the equivalent circuit model and the experimental data. The high-frequency intercept on the real axis in the Nyquist plots represents the solution/series resistance (R_s). The charge-transfer resistance (R_{ct}) connected with faradaic reactions at the electrode surface is represented by the depressed semicircle exhibited in the high-to-mid frequency region. Due to its inherently low electrical conductivity, the CeO_2 electrode displays a larger semicircle diameter, suggesting a greater R_{ct}. As a result of the conductive graphene network, which improves up electron transport and improves interfacial charge-transfer kinetics, the CeO_2/Graphene composite, on the other hand, exhibits a much smaller semicircle diameter, indicating a lower R_{ct}. The Nyquist plot's low-frequency area shows a straight line that approaches the imaginary axis, which is indicative of capacitive behavior and diffusion-controlled ion transport. Furthermore accordance with its better electrochemical performance, the CeO_2/Graphene electrode's steeper slope indicates better ion diffusion and a more optimal capacitive response.[49,50] The Bode phase angle charts for both electrodes are displayed in Fig. 13(c). When compared to pure CeO_2, the CeO_2/Graphene composite shows a larger phase angle in the low-frequency range, approximating the behavior of an ideal capacitive system. The graphene framework's dominating capacitive behavior and better charge storage reversibility are indicated by this enhanced phase response. The CeO_2/Graphene electrode exhibits a reduced impedance modulus ($|Z|$) across the entire frequency range, based to the Bode magnitude diagrams shown in Fig. 13(d). Specifically, the lowered impedance at high frequencies indicates improved electrical conductivity and decreased charge-transfer resistance, whereas the decreased impedance at low frequencies verifies quicker ion diffusion and lower internal resistance. These findings confirm graphene's advantageous function in enhancing the composite electrode's electrochemical kinetics.

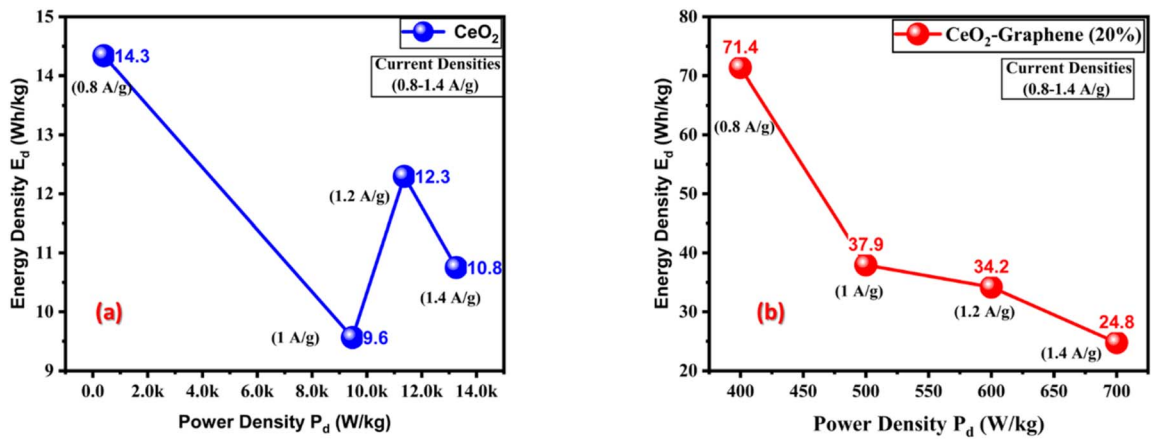

Fig. 12 Power density (P_d) (W kg^{-1}) *vs.* energy density (E_d) (Wh kg^{-1}) of CeO_2 and CeO_2/Graphene nanocomposite.

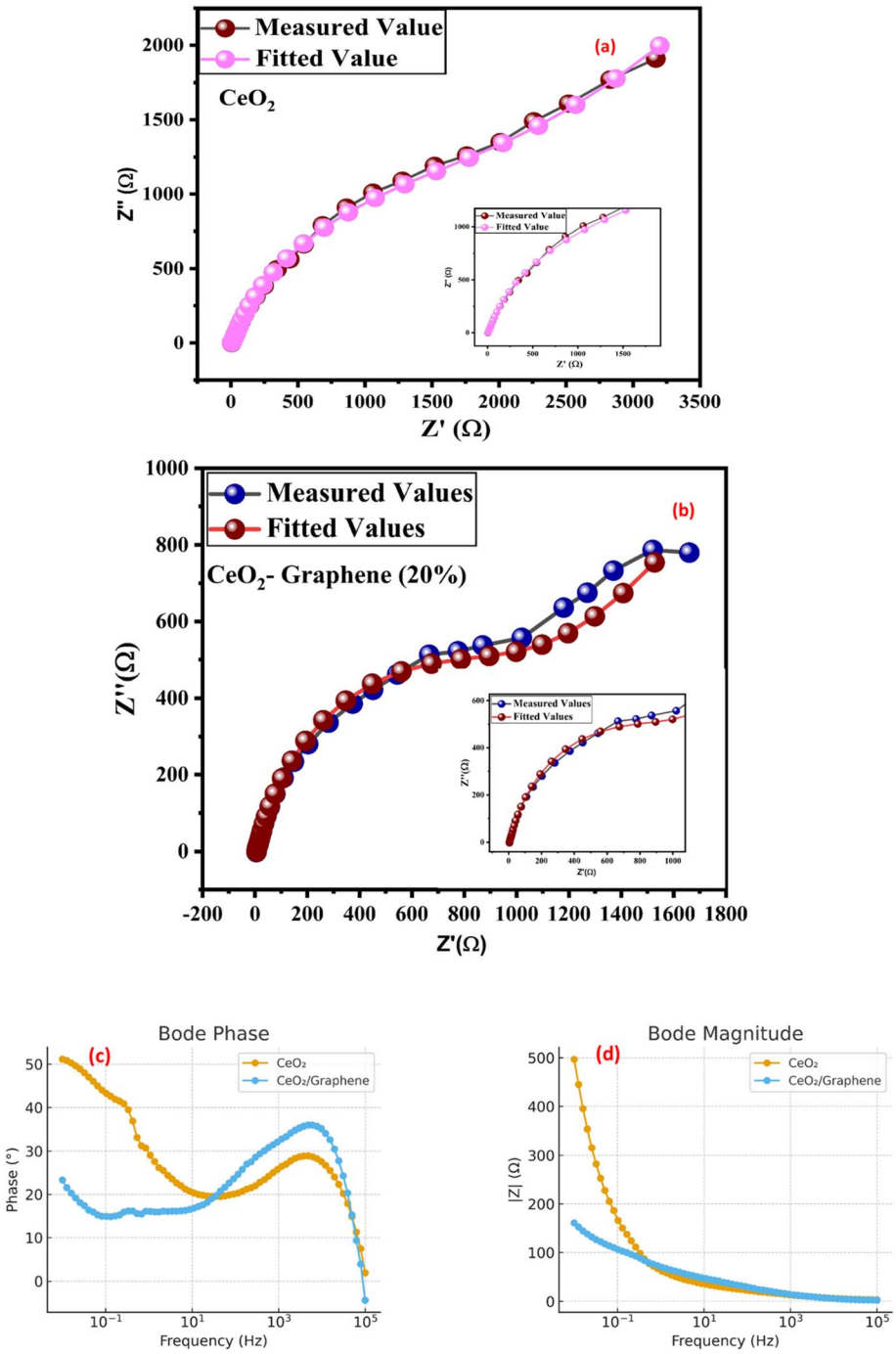

Fig. 13 EIS profile illustration of (a) CeO_2, (b) CeO_2/Graphene (c) Bode phase and (d) Bode magnitude.

The long-term reliability of the electrode materials was evaluated using repeated charge–discharge cycles, which is an important factor in supercapacitor dependability. Over 5000 continuous charge–discharge cycles, the electrodes' long-term cycling performance was evaluated (Fig. 14). After 5000 cycles at a constant current density, the CeO_2/Graphene composite retains around 91% of its original capacitance, demonstrating outstanding cycling stability. The conductive and flexible graphene framework, which prevents structural degradation of CeO_2 and preserves stable ion-accessible routes throughout repeated cycles, is responsible for this better retention. The pure CeO_2 electrode, on the other hand, only maintains around 74% of its initial capacitance. This is mainly because of increased internal resistance and low electrical conductivity, which hasten the deterioration of performance. The composite's improved electrolyte accessibility and interfacial electronic coupling between CeO_2 and graphene contribute to its increased electrochemical reversibility and long-term durability, demonstrating its applicability for high-performance supercapacitor applications.

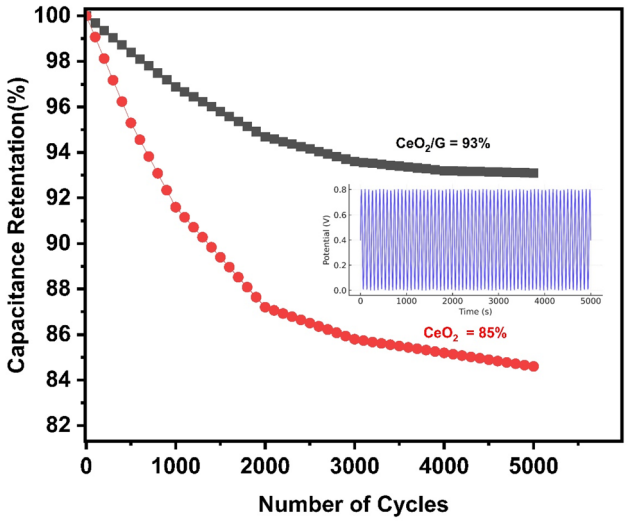

Fig. 14 Cycling stability of CeO_2 and CeO_2/Graphene electrodes.

The suggested charge-storage and defect-driven interfacial mechanism performing in the CeO_2/Graphene nanocomposite is shown in Fig. 15(a–d). Fig. 15(a) illustrates the CeO_2 lattice with a large number of oxygen vacancies produced during hydrothermal synthesis. A mixed Ce^+/Ce^{3+} valence state is produced by these defects, which increases redox activity and offers more electroactive sites for charge storage. Furthermore, vacancies reduce the ion-migration barrier, which makes it possible for electrolyte ions to interact with the ceria surface more effectively. The interfacial interaction between CeO_2 nanoparticles and the graphene sheet is seen in Fig. 15(b). At the interface, possible Ce–O–C interfacial interaction may contribute, producing an electrically linked route that facilitates quick electron transport from ceria to the highly conductive graphene network. By introducing localized electronic states and lowering CeO_2's effective bandgap, this interaction enhances the composite's charge-transfer kinetics. The charge-storage mechanism on the graphene-supported ceria nanoparticles is shown in Fig. 15(c). The CeO_2 surface is easily accessible to electrolyte ions (K^+), where reversible Ce^+/Ce^{3+} transitions lead to pseudocapacitive behavior. Electrons produced during these redox reactions are swiftly extracted by the conductive graphene scaffold, reducing recombination losses and facilitating effective use of active sites. Both specific capacitance and rate capability are improved by this cooperative effect. The entire composite architecture with evenly distributed CeO_2 nanoparticles attached on graphene layers is shown in Fig. 15(d). In addition to increasing the available surface area and preventing particle aggregation, this arrangement provides continuous electron-transport pathways across the graphene sheet. Additionally, smooth ion-diffusion channels are facilitated by wide space between nanoparticles, which lowers internal resistance and promotes stable long-term cycling.

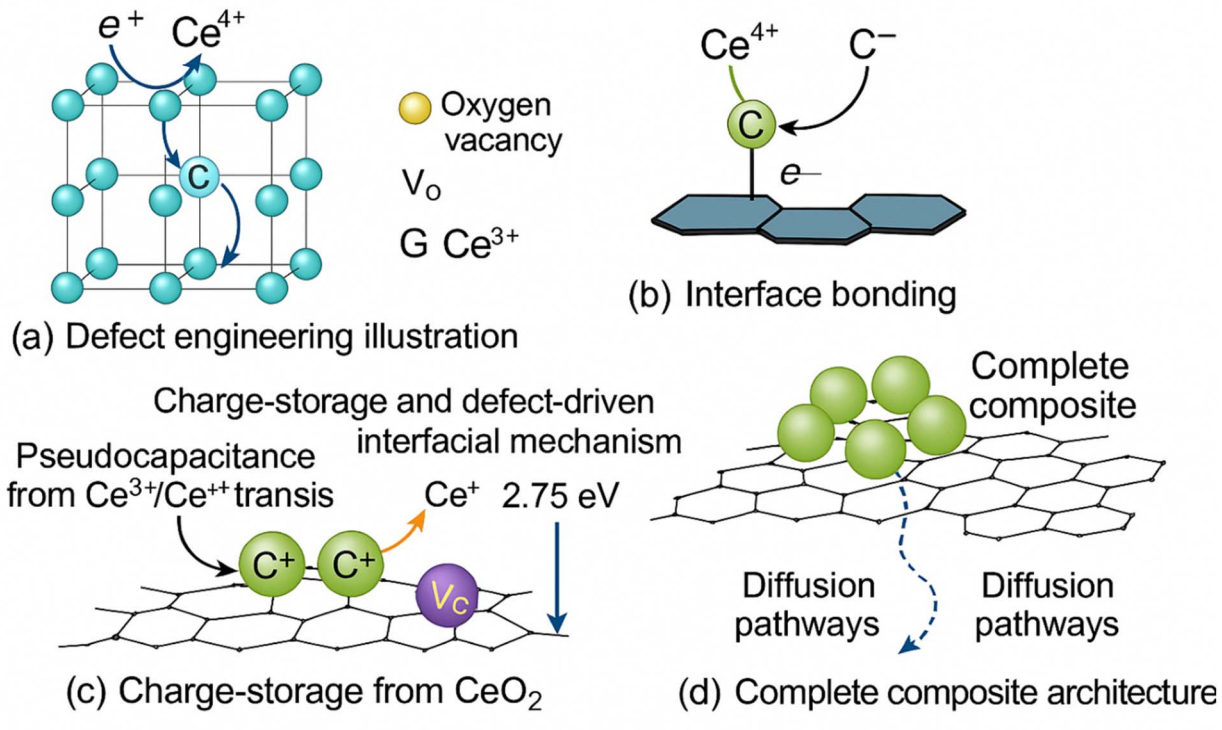

Fig. 15 (a–d) Schematic diagram of the CeO_2/Graphene nanocomposite's defect engineering, interfacial coupling, charge-storage routes, and ion-diffusion architecture.

Table 2 Comparative Evaluation of CeO_2/Graphene Supercapacitors

S no	Study	Synthesis route	Graphene/carbon role	Strengths	Limitations	Additional findings/mechanistic insight
1	Present work (2026)	Hydrothermal + electrochemical exfoliation graphene	Conductive scaffold + defect modulation	Simple, scalable, excellent CeO_2 anchoring; strong Ce–O–C interface; moderate C_{sp} (165–285 F g^{-1})	Slight agglomeration in pure CeO_2	Strong Ce^{3+}/Ce^{4+} redox, oxygen vacancy formation; large bandgap reduction; lowest R_{ct} among binary CeO_2/G; high ED (~5.7 Wh kg^{-1})
2	Britto *et al.*, 2020 (ref. 24)	Hydrothermal	Charge transport channels	Lower R_{ct} than CeO_2; mild improvement in conductivity	Low energy density; limited defect engineering	Graphene improves semicircle shrinkage in EIS; CeO_2 partially agglomerated
3	Yousef *et al.*, 2020 (ref. 25)	Chemical reduction	Conductive substrate (rGO flakes)	Good stability; optimized CeO_2 loading	Moderate C_{sp} (452 F g^{-1})	rGO improves double-layer contributions; CeO_2 content highly affects ionic diffusion
4	Salarizadeh *et al.*, 2021 (ref. 10)	Hydrothermal	Interfacial synergy	Good pseudocapacitance; decent cycling	Moderate capacitance range	FTIR confirms Ce–O–C bonding; electrode shows mixed EDLC + pseudocapacitive behavior
5	Wang *et al.*, 2011 (ref. 53)	*In situ* deposition	Conductive graphene network	Improved conductivity; ~200 F g^{-1}	Low C_{sp}; limited vacancy engineering	CeO_2 particle size relatively large (>20 nm); weak Ce–graphene bonding reduces faradaic activity
6	Dezfuli *et al.*, 2015 (ref. 56)	Sonochemical	rGO support + electron pathway	High stability (105% after 4000 cycles)	Csp only ~211 F g^{-1}	Cycling activation due to increased surface wetting; slow ion diffusion at higher scan rates
7	Sarpoushi *et al.*, 2014 (ref. 51)	Mechanical pressing	Graphene carrier	Simple method; Ce^{3+}/Ce^{4+} redox identifiable	Very low C_{sp} (~11 F g^{-1})	Poor interfacial contact; limited electrolyte penetration; no nanoscale engineering
8	Ji *et al.*, 2015 (ref. 52)	Hydrothermal	rGO support	Moderate C_{sp} (~89 F g^{-1}); good structural quality	Weak electrochemical activity	SAED shows partial crystallinity; rGO prevents CeO_2 aggregation but redox activity remains low
9	Vanitha *et al.*, 2015 (ref. 13)	Hydrothermal + Ag decoration	Graphene + Ag synergy	High C_{sp} (~700 F g^{-1}); improved conductivity	Uses noble metal; more complex synthesis	Ag nanoparticles introduce additional redox pathways; improved charge kinetics *via* Ag–CeO_2 coupling
10	Heydari *et al.*, 2017 (ref. 54)	Hydrothermal	N-doped rGO (NRGO)	Strong interfacial coupling; enhanced conductivity	C_{sp} < 600 F g; requires doping step	N-doping increases electron density and active sites; lower R_{ct} than undoped rGO systems
11	Jeyaranjan *et al.*, 2019 (ref. 55)	Hydrothermal + *in situ* polymerization (PANI/rGO/CeO_2)	Graphene scaffold + PANI pseudocapacitance	High C_{sp} (>600 F g^{-1}); good ED (~50 Wh kg^{-1})	Ternary system; stability issues for PANI	Ternary synergy: PANI adds pseudocapacitance; rGO improves conductivity; CeO_2 adds redox centers

4.4. Comparative evaluation of recently reported supercapacitor electrodes

The electrochemical performance of the presently available CeO_2/graphene (CeO_2/G) nanocomposite was thoroughly compared with previously published CeO_2/carbon electrode materials in order to further determine its importance (Table 2). Previous studies on CeO_2/graphene hybrids mostly used traditional hydrothermal or sonochemical techniques, which enhanced CeO_2 dispersion and electrical conductivity but only produced minimal capacitance values. For example, Britto *et al.* (2020)[24] reported enhanced electron transport but restricted energy density because of inadequate defect engineering in the CeO_2 matrix, whereas Jayashree *et al.* (2021)[23] reported a capacitance of 782 F g^{-1} for hydrothermally produced CeO_2 on graphene. Salarizadeh *et al.* (2021)[10] and Yousef *et al.* (2020)[25] both showed respectable cycle stability and pseudocapacitive behavior, still, their specific capacitances stayed below 500 F g^{-1}, suggesting that the active material's electrochemical usage was limited. Low-capacitance systems that achieve just 11–89 F g^{-1}, as reported by Sarpoushi *et al.* (2014)[51] and Ji *et al.* (2015),[52] further demonstrate that faradaic processes cannot be activated by simple mechanical mixing or weak CeO_2 carbon interfacial interaction. Due to poor Ce–O–C interactions and limited oxygen-vacancy production, which are crucial for charge-transfer kinetics, even the pioneering work by Wang *et al.* (2011),[53] in which CeO_2 nanoparticles were directly placed on graphene, only produced ~200 F g^{-1}. Higher capacitances in the range of 600–800 F g^{-1} were obtained by more sophisticated methods, such as Ag-decorated CeO_2/graphene (Vanitha *et al.*, 2015),[13] N-doped rGO–CeO_2 (Heydari *et al.*, 2017),[54] and ternary PANI/rGO/CeO_2 (Jeyaranjan *et al.*, 2019).[55] Nevertheless, these systems required conductive polymers or extra metal dopants, which raised the cost and complexity of manufacturing. With capacitances of 728–843 F g^{-1}, even high-performance Co–CeO_2/rGO and Ni–CeO_2/rGO ternary composites attained their increased activity mostly through multicomponent synergistic effects rather than CeO_2 carbon engineering alone. The current CeO_2/G electrode, on the other hand, provides a competitive specific capacitance of ~285 F g^{-1}, without the need of external dopants, noble metals, or polymeric additives. It is produced using a simple hydrothermal method in conjunction with electrochemical exfoliation of graphene. (i) Uniform nucleation of CeO_2 on defect-rich graphene sheets; (ii) Ce–O–C interfacial coupling enabling fast charge transfer; (iii) increased oxygen-vacancy concentration enhancing redox activity; and (iv) decreased charge-transport resistance within the composite architecture are all responsible for this exceptional performance. When compared to previously report binary CeO_2/graphene systems, these synergistic effects enable considerably higher electrochemical activity. Remarkably, they competitive among binary CeO_2/graphene systems without dopants that require more sophisticated manufacturing procedures.

5. Conclusions

In conclusion, the incorporation of graphene into CeO_2 to form a CeO_2/Graphene nanocomposite significantly enhances its electrochemical properties for supercapacitor applications. The composite's successful synthesis has been confirmed by structural and optical characterizations. The structural confirmation of the composite was further confirmed by Raman analysis, which directly demonstrated the development of defect-rich graphene (D and G bands) and oxygen-vacancy-containing CeO_2 (F_2g and defect modes). UV-visible spectroscopy showed changes in the absorption peaks, suggesting an enhanced charge transfer mechanism. The composite is ideal for energy storage applications because of its decreased optical band gap, which also promotes improved charge transfer and electronic conductivity. Electrochemical performance measured by Galvanic Charging–Discharging (GCD), Electrochemical Impedance Spectroscopy (EIS), and Cyclic Voltammetry (CV) revealed that the CeO_2/Graphene produced specific capacitance of 285 F g^{-1} at 0.8 A g^{-1}, significantly greater than pure CeO_2 (165 F g^{-1}), according to electrochemical studies, indicating effective use of redox-active sites and quicker electron/ion migration. According to the Ragone study, the composite obtained an energy density of 5.7 Wh kg^{-1} at a power density of 190 W kg^{-1}. The CeO_2/Graphene electrode retained around 91% of its capacitance after 5000 cycles, compared to approximately 74% for pure CeO_2, indicating a considerable improvement in cycling stability. The lower charge-transfer resistance caused by the conductive graphene network was further supported by the EIS data. Overall, this work highlights the potential of CeO_2/Graphene nanocomposites as promising electrode materials for next-generation supercapacitor devices by demonstrating that rational integration of graphene with CeO_2 is an effective strategy for improving charge storage capability and electrochemical stability.

Conflicts of interest

Authors declare no conflict of interest.

Data availability

All data supporting this study are available within the article.

Acknowledgements

This work was funded by the Ongoing Research Funding program (ORF-2026-492), King Saud University, Riyadh, Saudi Arabia.

References

1 D. Cai, D. Wang, B. Liu, Y. Wang, Y. Liu, L. Wang, H. Li, H. Huang, Q. Li and T. Wang, *ACS Appl. Mater. Interfaces*, 2013, **5**, 12905–12910.
2 H. Akbar, M. S. Javed, B. Parveen, A. Ahmad, A. Ali, M. R. Abukhadra, A. M. El-Sherbeeny and J. R. Choi, *J. Electrochem. Soc.*, 2025, **172**, 033501.
3 G. K. Veerasubramani, A. Chandrasekhar, Y. S. Mok and S. J. Kim, *J. Mater. Chem. A*, 2017, **5**, 11100–11113.

4 Y. Zou, X. Hu, H. Ma and S. E. Li, *J. Power Sources*, 2015, **273**, 793–803.
5 R. T. Yadlapalli, R. R. Alla, R. Kandipati and A. Kotapati, *J. Energy Storage*, 2022, **49**, 104194.
6 S. M. Benoy, M. Pandey, D. Bhattacharjya and B. K. Saikia, *J. Energy Storage*, 2022, **52**, 104938.
7 A. G. Olabi, Q. Abbas, A. Al Makky and M. A. Abdelkareem, *Energy*, 2022, **248**, 123617.
8 Y. Feng, H. Zhang, W. Li, L. Fang and Y. Wang, *J. Power Sources*, 2016, **301**, 78–86.
9 H. L. Ferreira, R. Garde, G. Fulli, W. Kling and J. P. Lopes, *Energy*, 2013, **53**, 288–298.
10 P. Salarizadeh, M. B. Askari, H. Beydaghi, M. Rastgoo-Deylami and S. M. Rozati, *J. Phys. Chem. Solids*, 2021, **159**, 110284.
11 G. Sun, X. Wang, W. Yu, N. Pei, W. Zhang, L. Sun, P. Yue, G. Zhang, P. Xiong and Q. Lu, *Adv. Funct. Mater.*, 2025, e18451.
12 W. Zhang, Q. Lu, G. Sun, Z. Chen, P. Yue, G. Zhang, B. Song and K. Song, *Nano Lett.*, 2025, **25**, 6092–6100.
13 M. Vanitha, P. Cao and N. Balasubramanian, *J. Alloys Compd.*, 2015, **644**, 534–544.
14 K. Dhamodharan and A. K. Singh, *Electrochim. Acta*, 2023, **466**, 143008.
15 M. Karnan, L. Durai, K. H. Prakash and S. Badhulika, *J. Energy Storage*, 2022, **56**, 106114.
16 H. Akbar, M. S. Akram, A. Ali and M. S. Javed, 2024.
17 N. Chakrabarty, A. Dey, S. Krishnamurthy and A. K. Chakraborty, *Appl. Surf. Sci.*, 2021, **536**, 147960.
18 Z. Yu, S. Wang, Y. Huang, Y. Zou, F. Xu, C. Xiang, J. Zhang, J. Xie and L. Sun, *J. Energy Storage*, 2022, **55**, 105486.
19 S. Arunpandiyan, S. Bharathi, A. Pandikumar, S. E. Arasi and A. Arivarasan, *Mater. Sci. Semicond. Process.*, 2020, **106**, 104765.
20 K. T. Kubra, R. Sharif, B. Patil, A. Javaid, S. Shahzadi, A. Salman, S. Siddique and G. Ali, *J. Alloys Compd.*, 2020, **815**, 152104.
21 T. Li and H. Liu, *Powder Technol.*, 2018, **327**, 275–281.
22 D. Deng, N. Chen, Y. Li, X. Xing, X. Liu, X. Xiao and Y. Wang, *Phys. E Low-dimens. Syst. Nanostruct.*, 2017, **86**, 284–291.
23 M. Jayashree, V. Sharmila, K. Meganathan, R. BoopathiRaja, M. Parthibavarman, M. Shkir and S. AlFaify, *Inorg. Chem. Commun.*, 2021, **132**, 108838.
24 S. Britto, V. Ramasamy, P. Murugesan, B. Neppolian and T. Kavinkumar, *Diamond Relat. Mater.*, 2020, **105**, 107808.
25 A. Yousef, A. M. Al-Enizi, I. M. Mohamed, M. El-Halwany, M. Ubaidullah and R. M. Brooks, *Ceram. Int.*, 2020, **46**, 15034–15043.
26 R. Baweja, M. Verma, S. Gautam, S. Upreti and N. Goyal, *RSC Adv.*, 2024, **14**, 17855–17865.
27 M. Ali, *Mater. Today Commun.*, 2023, **36**, 106552.
28 C. Liu, Y. Bai, Y. Zhao, H. Yao and H. Pang, *Energy Storage Mater.*, 2020, **33**, 470–502.
29 M. Ahmed, E. Ateia, L. Salah and A. El-Gamal, *Mater. Chem. Phys.*, 2005, **92**, 310–321.
30 H. Akbar, S. Akram, A. Ali and M. Subhan Javed, *Funct. Compos. Struct.*, 2024, **6**, 045011.
31 P. Rozhin, M. Melchionna, P. Fornasiero and S. Marchesan, *Nanomaterials*, 2021, **11**, 2259.
32 C. Wang, Z. Qin, K. Feng and B. Zhong, *J. Polym. Res.*, 2020, **27**, 1–10.
33 H. Akbar, A. Ali, S. Mohammad, F. Anjum, A. Ahmad, A. M. Afzal, M. D. Albaqami, S. Mohammad and J. R. Choi, *Molecules*, 2024, **29**, 2103.
34 A. Iqbal, A. S. Ahmed, N. Ahmad, A. Shafi, T. Ahamad, M. Z. Khan and S. Srivastava, *Environ. Nanotechnol. Monit. Manag.*, 2021, **16**, 100505.
35 N. Monica Ahmad and N. Aishah Hasan, *J. Nanotechnol.*, 2023, **2023**, 9572025.
36 G. Bai, J. Wang, Z. Yang, H. Wang, Z. Wang and S. Yang, *RSC Adv.*, 2014, **4**, 47096–47105.
37 A. Ambrosi and M. Pumera, *Chem. Eur J.*, 2016, **22**, 153–159.
38 S. Seal, A. Jeyaranjan, C. J. Neal, U. Kumar, T. S. Sakthivel and D. C. Sayle, *Nanoscale*, 2020, **12**, 6879–6899.
39 D. Mullins, S. Overbury and D. Huntley, *Surf. Sci.*, 1998, **409**, 307–319.
40 X. He, X. Liu, R. Li, B. Yang, K. Yu, M. Zeng and R. Yu, *Sci. Rep.*, 2016, **6**, 22238.
41 S. Nilawar, M. Bs and K. Chatterjee, *J. Polym. Environ.*, 2023, **31**, 2941–2955.
42 D. Toloman, A. Popa, R. B. Sonher, R. Bortnic, T. F. Marinca, I. Perhaita, M. Filip and A. Mesaros, *Appl. Sci.*, 2024, **14**, 522.
43 B. Sun, W. Chen, W. Zheng, H. Zhang, T. X. Liu, A. Elmarakbi and Y. Fu, *J. Catal.*, 2023, **424**, 106–120.
44 Q. Deng, Y. Yang, S. Qu, W. Wang, Y. Zhang, X. Ma, W. Yan and Y. Zhang, *Energy Storage Mater.*, 2021, **42**, 484–492.
45 A. Trentin, S. Harb, M. Uvida, K. Marcoen, S. Pulcinelli, C. Santilli, H. Terryn, T. Hauffman and P. Hammer, *Corros. Sci.*, 2021, **189**, 109581.
46 H. Shao, Z. Lin, K. Xu, P.-L. Taberna and P. Simon, *Energy Storage Mater.*, 2019, **18**, 456–461.
47 H. Akbar, M. S. Javed, S. T. Iqbal, M. I. Khan, T. Anwar, F. Anjum, A. Ahmad, M. Muneeb, A. Ali and W.-C. Oh, *J. Korean Ceram. Soc.*, 2024, **61**, 367–390.
48 F. Nemati, M. Rezaie, H. Tabesh, K. Eid, G. Xu, M. R. Ganjali, M. Hosseini, C. Karaman, N. Erk and P.-L. Show, *Environ. Res.*, 2022, **208**, 112685.
49 J. Qian, Y. Wang, Z. Chen, C. Liu, Y. Zhou, Y. Yang, Y. Song and B. Kong, *Inorg. Chem. Commun.*, 2019, **104**, 8–13.
50 V. Balasubramani, T. Sridhar and B. Liu, *Ceram. Int.*, 2024, **50**, 4359–4373.
51 M. R. Sarpoushi, M. Nasibi, M. A. Golozar, M. R. Shishesaz, M. R. Borhani and S. Noroozi, *Mater. Sci. Semicond. Process.*, 2014, **26**, 374–378.
52 Z. Ji, X. Shen, H. Zhou and K. Chen, *Ceram. Int.*, 2015, **41**, 8710–8716.
53 Y. Wang, C. X. Guo, J. Liu, T. Chen, H. Yang and C. M. Li, *Dalton Trans.*, 2011, **40**, 6388–6391.
54 H. Heydari and M. B. Gholivand, *Appl. Phys. A*, 2017, **123**, 187.
55 A. Jeyaranjan, T. S. Sakthivel, C. J. Neal and S. Seal, *Carbon*, 2019, **151**, 192–202.
56 A. S. Dezfuli, M. R. Ganjali, H. R. Naderi and P. Norouzi, *RSC Adv.*, 2015, **5**, 46050–46058.